**ORIGINAL PAPER**

# Adjusting the state of pitch anode for effective oxidation with suppressed graphitization and enhanced Na storage performances

Fangyu Li[1] · Huachao Tao[1] · Xuelin Yang[1]

## Abstract

Pitch has captured extensive interest as an anode material for sodium-ion batteries due to the abundant resources, low cost, and improvable reversible capacity through oxidation; however, not all the oxidations are effective. Here, a precise low-temperature pyrolysis strategy is successfully adopted to affirm the effective oxidation precursor. The results indicate that adjusting the state of pitch before oxidation can realize different structural conversions and Na storage performances during high-temperature carbonization. Carbonized pristine pitch (P-1400) and carbonized oxidized pitch, whose precursor is pyrolyzed at 600 °C (P600-N + S-1400), both show graphite-like microcrystallite structures and deliver reversible capacities 92.4 and 93.1 mAh $g^{-1}$ (at 20 mA $g^{-1}$) with 48.8 and 47.6% initial coulombic efficiencies, respectively. In comparison, carbonized oxidized pitch, whose precursor is pyrolyzed at 400 °C (P400-N + S-1400), displays a typical amorphous structure and increases the reversible capacity to 315.1 mAh $g^{-1}$ (at 20 mA $g^{-1}$) with 61.4% initial coulombic efficiency. Only incompletely carbonized pitch can have effective oxidation with suppressed graphitization and enhanced electrochemical performances.

**Keywords** Incompletely carbonized pitch · Sodium-ion battery · Oxidation · Suppressed graphitization · Enhanced electrochemical performances

## Introduction

Sodium-ion batteries (SIBs) have similar working principles and components to lithium-ion batteries (LIBs). Abundant resources, low costs, and safety performances make SIB promising in the field of large-scale energy storage [1, 2]. Surprisingly, graphite, which is a kind of carbon anode with excellent electrochemical performances and mature commercial application in LIB [3], is difficult to insert/extract for $Na^+$ due to thermodynamics [4, 5]. It prompts researchers to pay more attention to other carbon materials [6–18]. Compared with hard carbon with a higher specific capacity but higher cost, researchers are still searching for better-performed soft carbon through tuning and optimizing the structures [19–23].

✉ Xuelin Yang
  xlyang@ctgu.edu.cn

1  Hubei Provincial Collaborative Innovation Center for New Energy Microgrid, College of Electrical Engineering & New Energy, China Three Gorges University, Yichang 443002, China

Many precursors have been used to synthesize soft carbon, including petroleum coke, pitch, plastics, tar, and most aromatic compounds [7, 24–29]. Among them, pitch has a low price [30]. However, pitch is also abundant with oligomers of alkylated polycyclic aromatic hydrocarbons. The direct pyrolysis of pitch at high temperatures results in soft carbon with near parallel stacked carbon sheets and a relatively high graphitization degree, which is unsuitable for $Na^+$ insertion/extraction [31].

Fortunately, it has been reported that oxidation can effectively stabilize the molecule structure of pitch and prevent its softening through forming the cross-linking networks during carbonization [32–36]. It results in more disordered crystalline structures with enlarged interlayer spacing, which exhibits the typical Na storage behavior of hard carbon. Based on previous researches [6, 32, 37, 38], the formation of cross-linking networks is favored by the presence of oxygen or shortage of hydrogen in the raw carbon materials. During the early stage of carbonization, carbon materials with much hydrogen can constantly form hydrocarbon decomposition products, which will prevent carbon materials from solid state and remain relatively mobile, inducing a continual

reduction and destruction of cross-links. By contrast, if the carbon residue remains few hydrogens after the first mass loss at the early stage of carbonization, the voids formed by the gas escape would not be able to collapse, leading to solid-state carbonization and non-graphitization at further high temperatures [37–39].

Recently, Qi et al. presented an in situ $Mg(NO_3)_2 \cdot 6H_2O$ solidification strategy for pitch to convert the fusion-state into solid-state carbonization [40]. The oxygen species and solid products generated from the decomposition of $Mg(NO_3)_2 \cdot 6H_2O$ retarded the melting and reordering of pitch. Furthermore, the comparison experiment of $Fe(NO_3)_3 \cdot 9H_2O$ proposed that not all the oxidations are effective. Only by providing oxygen within an appropriate temperature range can the excess hydrogen be neutralized, preventing the melting at the initial stage of pitch carbonization. Compared with the traditional oxidation method, this research provides a new thought that using the continuous decomposition of $Mg(NO_3)_2 \cdot 6H_2O$ can supply oxygen during carbonization. Nevertheless, it also raises a question: how to reach the appropriate oxidation temperature range for pitch?

Here, a series of pitch-based carbon for SIB anodes via low-temperature pyrolysis, oxidation, and high-temperature carbonization were prepared. A precise low-temperature pyrolysis strategy, which adjusted the pyrolysis temperature over a wide range of 0~800 °C, was adopted to affirm the effective oxidation precursor. The results reveal that adjusting the state of pitch before oxidation can realize different structural conversions and Na storage performances during high-temperature carbonization. Only by oxidizing incompletely carbonized pitch can the non-graphitizing carbon be formed after carbonization, exhibiting the superior reversible capacity and initial coulombic efficiency (ICE) for SIB.

# Experimental

## Material synthesis

The pristine pitch (P, Canrd) was firstly heated under argon treatment at different temperatures (200 °C, 300 °C, 400 °C, 500 °C, 600 °C, and 800 °C) for 2 h to get different states of pitch-based carbon (P, P200, P300, P400, P500, P600, and P800). Then, pitch-based carbon was dispersed in the mixture of sulfuric acid ($H_2SO_4$, 95.0~98.0%) and nitric acid ($HNO_3$, 65.0~68.0%), respectively, keeping $V(H_2SO_4)/V(HNO_3) = 1{:}2$. After stirring at 50 °C for 12 h, washing with deionized water, and heating at 80 °C for 24 h, the oxidation products (P-N + S, P200-N + S, P300-N + S, P400-N + S, P500-N + S, P600-N + S, and P800-N + S) were obtained. Finally, the dried oxidation products were annealed at 1400 °C for 2 h under flowing argon, and

the target products (P-N + S-1400, P200-N + S-1400, P300-N + S-1400, P400-N + S-1400, P500-N + S-1400, P600-N + S-1400, and P800-N + S-1400) were synthesized. The optimal carbonization temperature was 1400 °C with the best electrochemical performances after oxidation [35].

As the pitch-based carbon in this experiment was heated twice, namely low-temperature pyrolysis and high-temperature carbonization, carbonized pitches with different pyrolysis temperatures and an identical carbonization temperature were tested to confirm whether pyrolysis temperature affects the electrochemical performances of pitch. Comparing the galvanostatic charge/discharge curves (the first cycle, 20 mA g$^{-1}$) in Fig. S1, it showed that the reversible capacities of carbonized pitches with different pyrolysis temperatures were nearly the same. Therefore, different pyrolysis temperatures did not affect the experimental data in this paper.

## Material characterization

High-resolution transmission electron microscopy (HRTEM) and selected area electron diffraction (SAED) measurements were performed on a JEOL-F200. X-ray diffraction (XRD) was analyzed on a Rigaku Ultima IV. Raman spectra were obtained on a Thermo Scientific DXR. Fourier transform infrared spectroscopy (FTIR) measurements were performed on a Frontier NIR. X-ray photoelectron spectra (XPS) were performed on a Shimadzu AXIS Supra. Thermogravimetry (TG) and differential scanning calorimeter (DSC) were carried on an STA 449 F5.

## Electrochemical measurements

The electrochemical tests were conducted on CR2025 coin cells at ambient temperature. The working electrode was prepared by spreading the homogeneous slurry onto a copper foil, which consisted of 80% active materials, 10% acetylene black, and 10% PVDF in N-methyl-2-pyrrolidone. Sodium metal was utilized as the counter electrode in SIB, and potassium metal was utilized as the counter electrode in potassium-ion battery (PIB). Glass fiber filters (GF/D) were used as the separator. The electrolyte in SIB was 1 M $NaClO_4$ with 2% fluoroethylene carbonate (FEC) additive dissolved in a mixture of ethylene carbonate, dimethyl carbonate, and ethyl methyl carbonate (EC/DMC/EMC = 1:1:1, vol%). The electrolyte in PIB was 0.8 M $KPF_6$ in a mixture of ethylene carbonate and diethyl carbonate (EC/DEC = 1:1, vol%). The coin cells were assembled in an Ar-filled glovebox (Mikrouna, $H_2O$, $O_2 < 0.1$ ppm). Galvanostatic charge/discharge curves, rate performances, and cycling performances were obtained within the potential range of 3.00~0.01 V (vs. Na$^+$/Na) and 3.00~0.01 V (vs. K$^+$/K) on a Land CT2001A battery tester. Cyclic voltammetry (CV) and electrochemical

impedance spectroscopy (EIS) were conducted using a CHI604E electrochemical workstation.

## Results and discussion

To analyze the structural conversions from oxidation, HRTEM, XRD, and Raman analyses of P400-N + S-1400, P600-N + S-1400, and P-1400 were performed. Apparent long-range-ordered parallel carbon layers are shown in HRTEM images (Fig. 1a, c), which reveal the high graphitization degrees of P-1400 and P600-N + S-1400. SAED patterns show sharp diffraction rings, which also demonstrate

the graphitic structures of P-1400 and P600-N + S-1400 [37, 41]. Oppositely, P400-N + S-1400 in Fig. 1b has a different microstructure. The disordered turbostratic structure with curved carbon layers becomes evident over the entire area, giving rise to a large number of voids due to layer shifting or folding with each other from the atomic mobility. Moreover, the diffraction ring in the corresponding SAED pattern is blurred, indicating the disordered structure of P400-N + S-1400 [42, 43].

XRD patterns (Fig. 1d) of P400-N + S-1400 and P600-N + S-1400 are also different. P400-N + S-1400 has a broad diffraction peak at $2\theta \approx 23.46°$ (Table 1), corresponding to the (002) plane, which is a characteristic of a
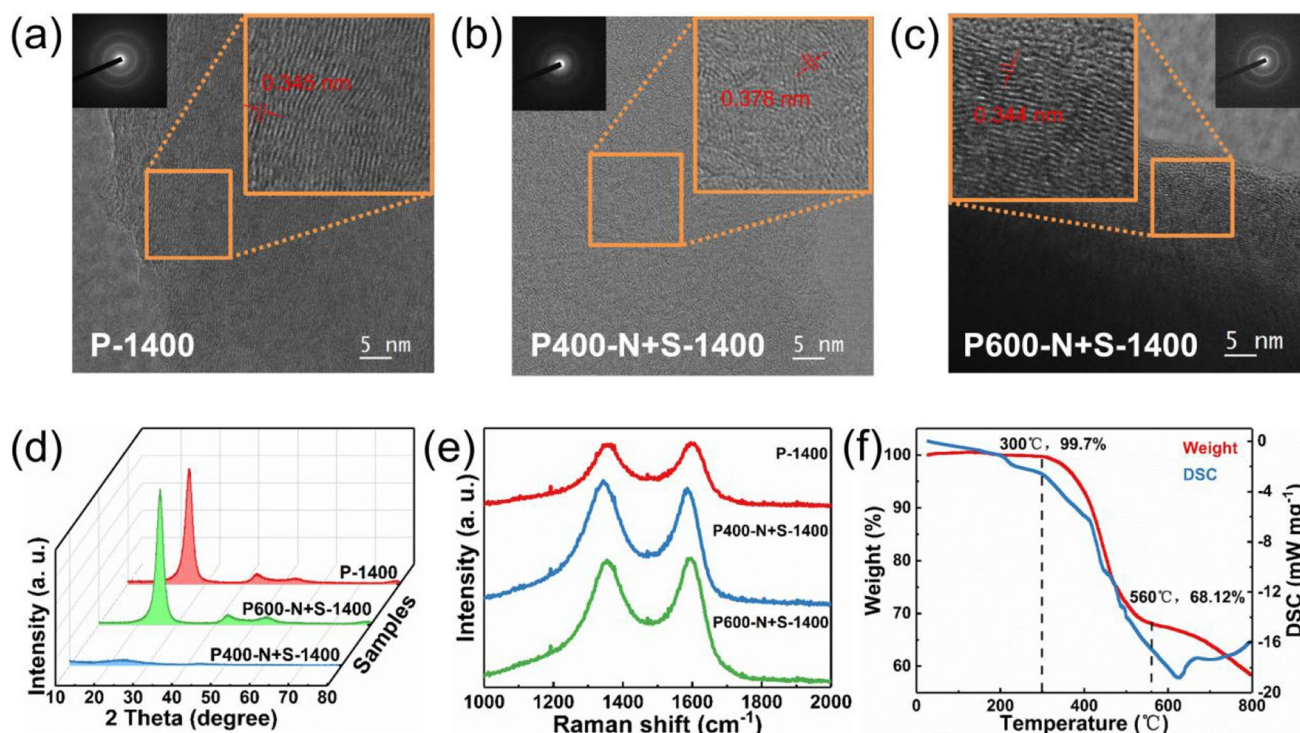


**Fig. 1** HRTEM images of **a** P-1400, **b** P400-N + S-1400, and **c** P600-N + S-1400. **d** XRD patterns and **e** Raman spectra of P-1400, P400-N + S-1400, and P600-N + S-1400. **f** TG curve of pitch under $N_2$ atmosphere

**Table 1** Physical parameters of samples from XRD, Raman, and XPS

| Samples | (002) peak (°) | $d_{002}$ (nm) | $I_D/I_G$ | C1s (at.%) | O1s (at.%) | N1s (at.%) | Atomic (%) | | |
|---|---|---|---|---|---|---|---|---|---|
| | | | | | | | C–O | C=O | C–OH |
| P400 | 24.76 | 0.359 | 0.55 | 95.59 | 4.41 | - | 0.54 | 0.58 | 0.52 |
| P600 | 25.52 | 0.349 | 0.61 | 90.94 | 9.96 | - | 1.04 | 1.67 | 1.18 |
| P400-N + S | 23.24 | 0.382 | 0.69 | 70.67 | 21.87 | 7.46 | 1.71 | 3.44 | 3.59 |
| P600-N + S | 25.46 | 0.350 | 0.71 | 81.75 | 15.56 | 2.69 | 0.98 | 3.84 | 1.35 |
| P400-N + S-1400 | 23.46 | 0.379 | 1.07 | 89.93 | 10.07 | - | - | - | - |
| P600-N + S-1400 | 25.74 | 0.346 | 0.99 | 93.53 | 6.47 | - | - | - | - |
| P-1400 | 25.80 | 0.345 | 0.99 | 95.27 | 4.73 | - | - | - | - |

typical amorphous structure. In contrast, the (002) peak of P600-N + S-1400 is quite sharp and symmetric, which is similar to P-1400, revealing graphite-like microcrystallite structures [37, 41, 43, 44]. The carbon layer spacings ($d_{002}$) calculated from the XRD data are shown in Table 1, which are consistent with the HRTEM results (Figs. 1a–c and S2-4). XRD patterns of other carbonized oxidized pitches are shown in Fig. S5. P-N + S-1400, P200-N + S-1400, and P300-N + S-1400 all indicate typical amorphous structures, the same with P400-N + S-1400. P800-N + S-1400 is graphitized just like P-1400 and P600-N + S-1400. P500-N + S-1400 is likewise graphitized, whereas the intensity of (002) peak is much lower than that of P-1400 and P600-N + S-1400, indicating P500-N + S-1400 is at the transition stage from a highly disordered structure to graphite-like structure. Raman spectra are presented in Fig. 1e. The intensity of D band is stronger than that of G band in P400-N + S-1400, while the situations are entirely inverse for P-1400 and P600-N + S-1400, which confirms the higher disorder degree of P400-N + S-1400 [35].

TG curves (Fig. 1f) were obtained to understand the state conversion of pitch. Weight loss is slight up to 300 °C due to the water desorption and the loss of methylene hydrogen. Evident weight loss is observed between 300 and 560 °C, indicating that pitch decomposes rapidly during this temperature as processes like molecule volatilization, hydrocarbon skeleton cleavage, as well as functional group partially abstraction may occur. After 560 °C, a polymerization reaction occurs and molecules are rearranged [45]. The weight loss becomes less apparent, revealing the carbonization of pitch has been completed [35].

Pitch is a kind of soft carbon, which is easy to convert amorphous carbon into graphite when the temperature is above 2500 °C [37]. The above results reveal that not all the oxidations can restrain the graphitization of pitch at high temperatures. Only incompletely carbonized pitch can maintain the amorphous structure after oxidation and carbonization, just like P, P200, P300, and P400. When pitch is carbonized at 500 °C, P500 is at the transition stage and its carbonized oxidized pitch is graphitized with low intensity.

When pitch is completely carbonized, such as P600 and P800, carbonized oxidized pitch turns to a graphite-like microcrystallite structure.

The changes caused by the introduction of oxygen were further analyzed. XRD patterns in Fig. 2a show that (002) peak of P400 is poorly crystallized, and a small bump is in the range of 10 ~ 20°. Compared with P400, P600 has a right shift (002) peak, and the bump is disappeared. It indicates that P400 is incompletely carbonized and P600 is completely carbonized [46], which is in correspondence with TG analysis. Compared with P400, (002) peak of P400-N + S shifts to the left and retains an amorphous structure, demonstrating an increased interlayer spacing of P400-N + S (Table 1). Unlike P400 series of carbon, only minute differences of (002) peaks are noticed between P600 and P600-N + S. In addition, typical broad amorphous carbon diffraction peaks corresponding to the (002) plane are all displayed in XRD patterns for pitch-based carbon and oxidized pitch-based carbon, indicating that the overall structure does not change after oxidation. Raman spectra in Fig. 2b present that the values of intensity ratio ($I_D/I_G$, Table 1) for P400, P400-N + S, P600, and P600-N + S are 0.55, 0.69, 0.61, and 0.71, respectively, indicating that the oxidized pitch-based carbon has higher $I_D/I_G$ values, which is an evolution of local structure from ordered to disordered after oxidation [35].

FTIR (Fig. 3a) measurement was conducted to affirm the existing state of oxygen. The peaks at around 3436 cm$^{-1}$ correspond to the O–H stretching vibration of hydroxyl groups and residual water. The peaks at approximately 1735 cm$^{-1}$ represent carboxyl/carbonyl stretching groups. Besides, the peaks occurring at 1343 cm$^{-1}$ are due to the O–H bending deformation of C–OH groups, and the C–O stretching vibrations are detected at 1032 cm$^{-1}$ [47]. It can be noticed in P400 series of carbon and P600 series of carbon that oxygen-containing groups such as C = O, C–O, and C–OH are all increased after oxidation, while the intensities are different. It could be tentatively concluded that the introduction of oxygen is mainly in the form of carboxyl after oxidation [48, 49]. Oxygen-containing groups are both introduced into P400-N + S and P600-N + S, just in different amounts.



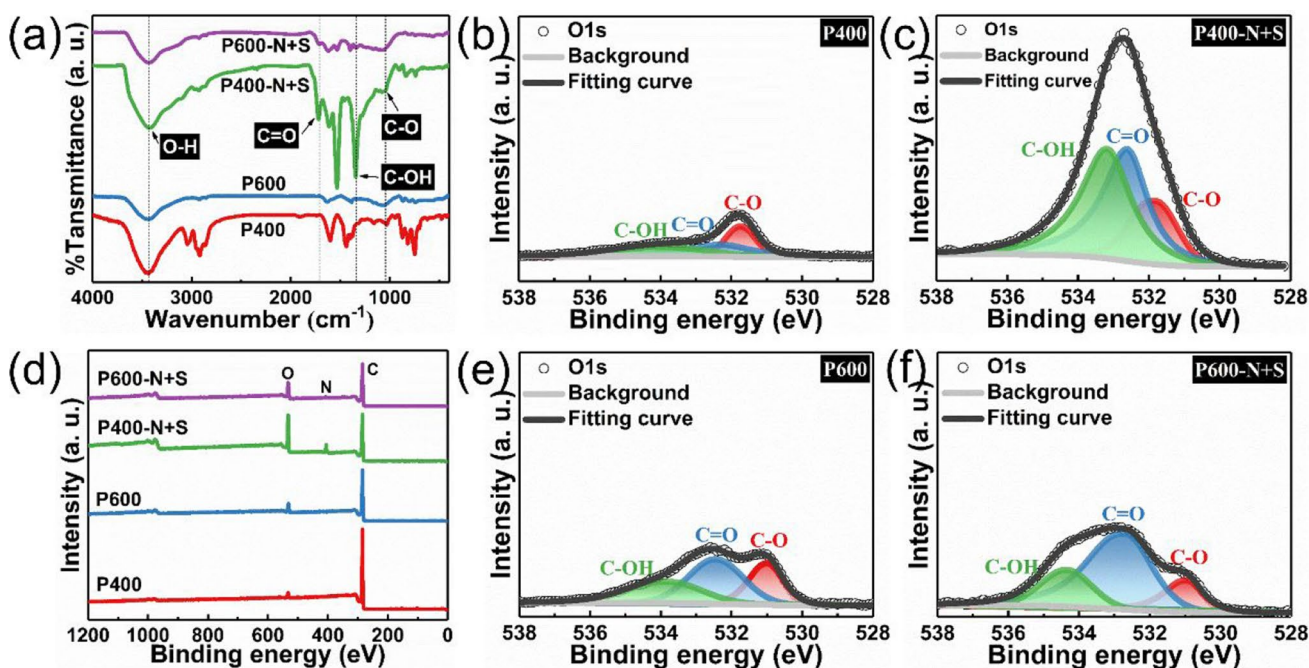Fig. 2 a XRD patterns and b Raman spectra of P400, P600, P400-N + S, and P600-N + S
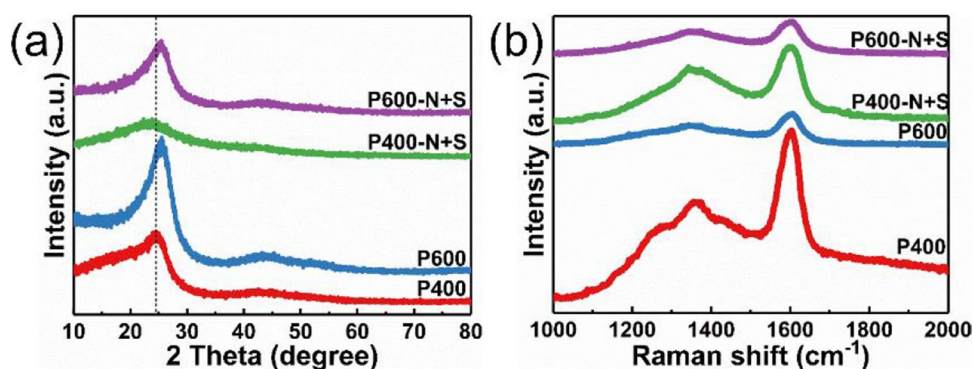
**Fig. 3** **a** FTIR spectra and **d** XPS survey spectra of P400, P600, P400-N + S, and P600-N + S. High-resolution O1s spectra of **b** P400, **c** P400-N + S, **e** P600, and **f** P600-N + S

XPS was collected to further understand the nature of corresponding bonds. XPS survey spectra (Fig. 3d) show that the content of O1s in P400-N + S is 21.87 at.% (Table 1), which is higher than that in P400 (4.41 at.%). High-resolution O1s spectra of P400-N + S (Fig. 3c) changes to higher binding energy than that of P400 (Fig. 3b), with three peaks denoting C=O, C–O, and C–OH being deconvoluted. The amounts of C–O, C=O, and C–OH in P400 are 0.54, 0.58, and 0.52 at.%, while those in P400-N + S are 1.71, 3.44, and 3.59 at.%, respectively. It demonstrates that P400-N + S contains more oxygen-containing groups than P400, especially C=O and C–OH [35, 47]. Compared to P600, the content of O1s in P600-N + S has a rise, which is from 9.96 to 15.56 at.%. The amounts of C=O and C–OH in P600 series of carbon also increase from 1.67 and 1.18 (Fig. 3e) to 3.84 and 1.35 at.% (Fig. 3f) after oxidation, respectively. In addition, the content of O1s in P400-N + S-1400 and P600-N + S-1400 is both higher than that in P-1400, which is 10.07, 6.47, and 4.73 at.%, respectively. Therefore, oxygen is picked up and mainly presents in carboxyl after oxidation. The growths of oxygen-containing groups are quite huge in P400-N + S, while those in P600-N + S are barely visible.

In conclusion, the oxidation effects on P400 series of carbon and P600 series of carbon are diverse. Lots of carboxyl are introduced into P400-N + S after oxidation, resulting in more small molecules (such as $H_2O$, CO, and $CO_2$) volatilizing with the decomposition of oxygen-containing groups during the high-temperature carbonization [40, 46, 50]. The

loss of more hydrogen contributes P400-N + S-1400 to form cross-linking networks and remain the amorphous structure [35, 37, 39]. Oppositely, oxidation has a limited effect on P600-N + S-1400. The completely carbonized pitch P600 has achieved fusion-state carbonization. Decreasing the hydrogen of P600 through oxidation to convert the fusion-state into solid-state carbonization is impossible. Most of the oxygen-containing groups introduced into P600-N + S after oxidation are decomposed into volatile substances during the high-temperature carbonization, and the rest causes a slight increase of oxygen in P600-N + S-1400. The carbonization process of P600 series of carbon is still a gradual graphitization of pitch at high temperatures.

The verified structure variations undoubtedly influence electrochemical performances. CV curves at different scanning rates of P-1400, P400-N + S-1400, and P600-N + S-1400 are shown in Fig. 4a–c. The curves of P-1400 and P600-N + S-1400 are quite distinct from those of P400-N + S-1400. P-1400 and P600-N + S-1400 have wide humps as the redox peaks, which are particularly evident at high scanning rates. The redox peaks of P400-N + S-1400 are a pair of sharp peaks at about 0.1 V, which is similar to the CV curve of a typical hard carbon anode, indicating the Na storage in P400-N + S-1400 has changed apparently and resembles the mechanism of hard carbon. Moreover, Fig. 4d, f suggests that P-1400 and P600-N + S-1400 have linear relations between peak current ($I_p$) and the square root of scanning rate ($v^{1/2}$), which
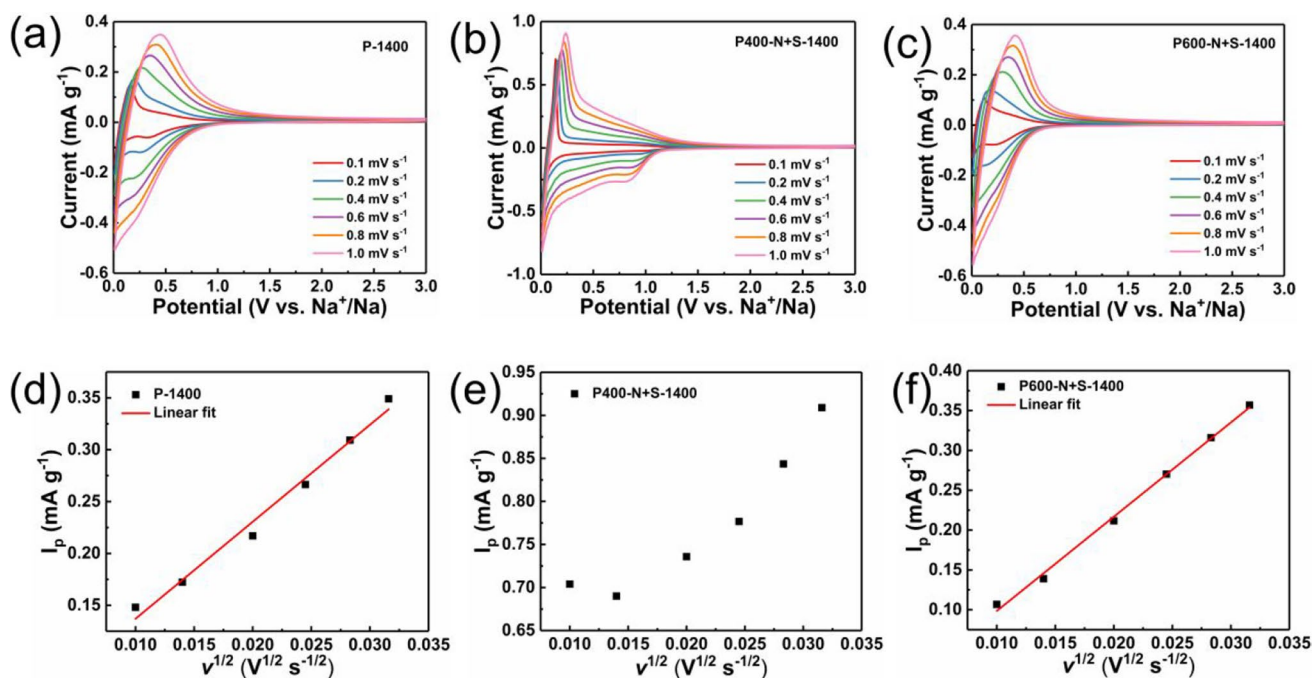
**Fig. 4** CV curves at different scanning rates of **a** P-1400, **b** P400-N + S-1400, and **c** P600-N + S-1400. Corresponding $I_p$-$v.^{1/2}$ relationship of **d** P-1400, **e** P400-N + S-1400, and **f** P600-N + S-1400

conforms to the Randles–Sevcik equation [51]. The corresponding $I_p$-$v^{1/2}$ relationship of P400-N + S-1400 (Fig. 4e) cannot fit linearly, revealing the unlike diffusion behavior of Na$^+$.

Galvanostatic discharge/charge measurements (Fig. 5a) conducted between 3.00 and 0.01 V versus Na$^+$/Na at a rate of 20 mA g$^{-1}$ were observed. The obtained P400-N + S-1400, P600-N + S-1400, and P-1400 deliver
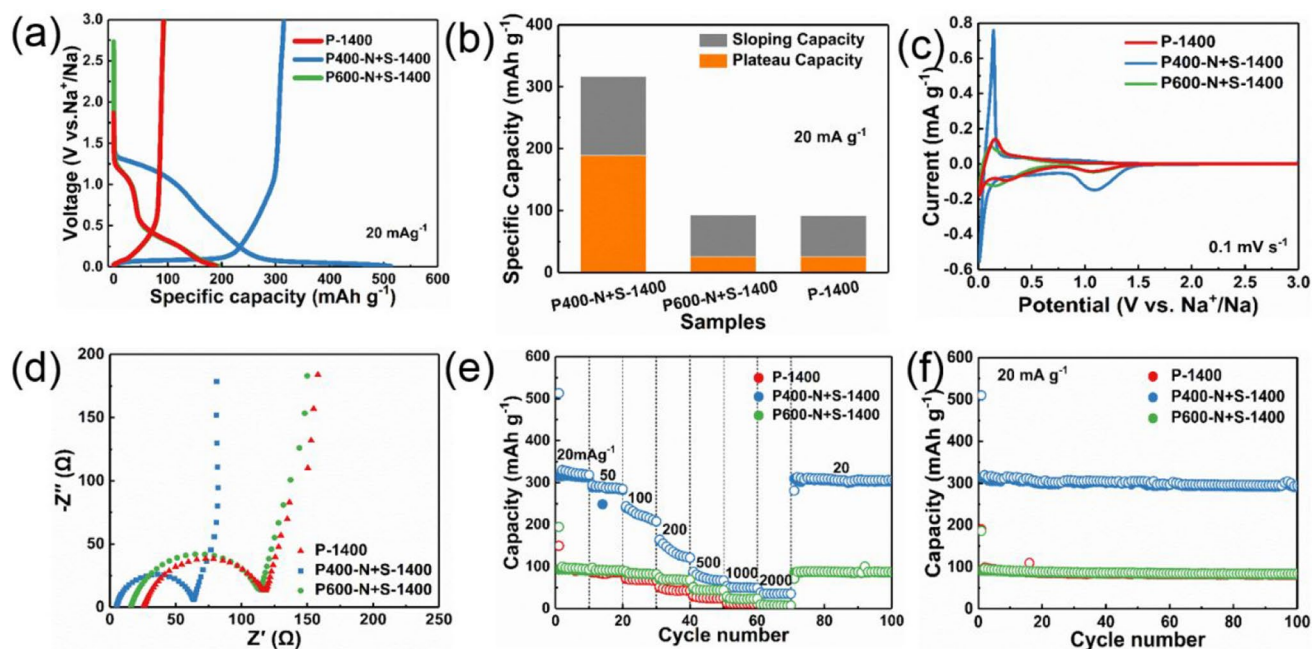


**Fig. 5** **a** Galvanostatic charge/discharge curves (the first cycle), **b** charge capacities (the third cycle) from the sloping-voltage and plateau-voltage regions, **c** CV curves (the first cycle), **d** EIS, **e** rate performances, and **f** cycling stabilities of P-1400, P400-N + S-1400, and P600-N + S-1400

reversible capacities of 315.1, 93.1, and 92.4 mAh g$^{-1}$ with 61.4, 47.9, and 48.8% ICE, respectively. P-1400 and P600-N + S-1400 basically show the sloping region, corresponding to the Na$^+$ interlayer intercalation due to the graphite-like structure and wide humped redox peaks of soft carbon [6, 24, 26, 44]. P400-N + S-1400 displays the sloping and 0.1 V plateau regions. Based on the mechanism of hard carbon [52, 53], the plateau region results from interlayer intercalation, and the sloping region is associated with defect adsorption. Galvanostatic discharge/charge curves of other carbonized oxidized pitches are shown in Fig. S6. After oxidation and carbonization, incompletely carbonized pitches enhance the Na storage performances and other carbonized pitches have limited improvement, corresponding to the microstructure analysis.

The dependence of the reversible capacity and the corresponding contribution from the sloping and 0.1 V plateau regions on different samples are plotted in Fig. 5b. The plateau capacity of P400-N + S-1400 is 189.2 mAh g$^{-1}$ at 20 mA g$^{-1}$, accounting for 59.7% of its total reversible capacity, which is much higher than that of P600-N + S-1400 and P-1400. It reveals that the plateau region contributes to the enhanced reversible capacity of P400-N + S-1400 [35].

Correspondingly, the CV curves of P400-N + S-1400, P600-N + S-1400, and P-1400 at 0.1 mV s$^{-1}$ (Fig. 5c and Fig. S7-9) show a regular evolution. All the curves have an irreversible 1.1 V reduction peak, which is generally attributed to the electrolyte decomposition and the formation of a solid electrolyte interface (SEI) film on the electrode surface [25]. Among the CV curves, P400-N + S-1400 has a pair of obvious 0.1 V redox peaks, indicating a high plateau capacity [6]. As P-1400 and P600-N + S-1400 are graphitized carbon, an overall higher sodiation potential of the quasi-plateau induces the reversible reduction peak at around 0.3 V [24].

EIS analysis (Fig. 5d) was carried out between 10 mHz and 100 kHz by applying an AC perturbation signal of 5 mV to check the impedances of cells with P400-N + S-1400, P600-N + S-1400, and P-1400 anode materials. The corresponding Nyquist plots of P600-N + S-1400 and P-1400 are nearly the same, both possessing larger semicircles than those of P400-N + S-1400. It indicates that the cell with P400-N + S-1400 anode has a smaller internal resistance, resulting from the decomposition of electrolytes and formation of the SEI film, which is consistent with the improved ICE [35, 54].

The rate capability of P400-N + S-1400, P600-N + S-1400, and P-1400 is shown in Fig. 5e. The reversible capacity of P400-N + S-1400 maintains 91.7% of the initial reversible capacity at 50 mA g$^{-1}$, remains 26.9% of the initial reversible capacity at 500 mA g$^{-1}$, and recovers 98.3% of the initial reversible capacity at 20 mA g$^{-1}$ after experiencing 2000 mA g$^{-1}$, indicating an inferior rate capability, which is in accord with the performance of typical hard carbon anode. As for the cycling stabilities (Fig. 5f), the performances of all the samples seem close to each other, maintaining around 90% of the initial reversible capacity at 20 mA g$^{-1}$ over 100 cycles.

Nevertheless, it is worth noting that the electrochemical performances of P600-N + S-1400 and P-1400 are not selfsame, although the low capacity makes the improvement not apparent. As graphitized carbon is better for the storage of K$^+$ [55–63], the improvement of P600-N + S-1400 anode was measured in PIB. In Fig. 6a, P600-N + S-1400 and P-1400 deliver reversible capacities 252.6 and 233.6 mAh g$^{-1}$ (at 20 mA g$^{-1}$) with 56.9 and 51.8% ICE in PIB, respectively. With an increased rate, the reversible capacity of P-1400 downs faster than P600-N + S-1400 and even stops at 1000 mA g$^{-1}$. P600-N + S-1400 recovers the capacity of 20 mA g$^{-1}$ after experiencing 1000 mA g$^{-1}$ high rate discharge, however, with a serious capacity fading in the later cycles. The capacity fading of P600-N + S-1400 and P-1400 during cycling at 200 mA g$^{-1}$ (Fig. 6b) are obvious, like other carbon anodes in PIB [56, 59, 64–67]. It is clear that oxidation improves the electrochemical performances of P600-N + S-1400 in PIB, corresponding to the results of oxygen in XPS since oxygen can be seen as a doping to improve K$^+$ transport and increase storage sites [59]. Obviously, oxidation has a slight effect on the microstructure of P600-N + S-1400, making it not exactly identical with P-1400 and resulting in the corresponding variation in electrochemical performances.



**Fig. 6** **a** Rate performances and **b** cycling stabilities of P-1400 and P600-N + S-1400 in PIB
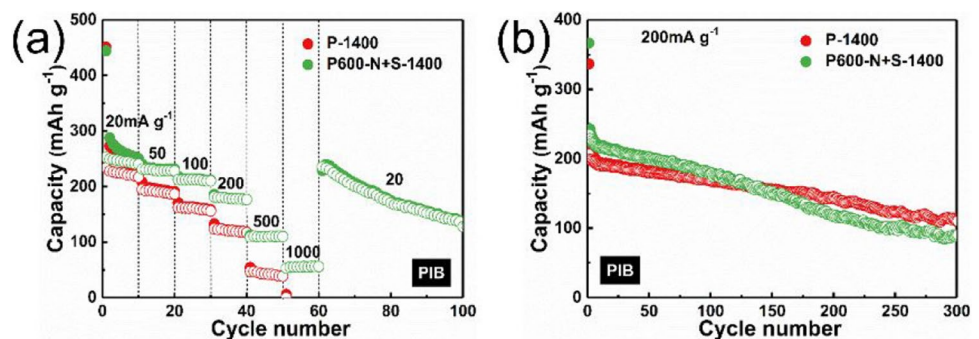
Linking the interpretation of microstructure with Na storage performances, it is affirmed that the state of pitch before oxidation plays a key role in suppressing the graphitization and improving the electrochemical performances. After oxidation and high-temperature carbonization, the incompletely carbonized pitch has superior Na storage performances with an amorphous structure. Oppositely, the completely carbonized pitch is gradually graphitized, inducing the reversible capacity similar to that of the carbonized pristine pitch.

Specifically (Fig. 7), when the pyrolysis temperature is lower than complete carbonization temperature ($T_p$), pitch turns to incompletely carbonized pitch with basically constant structure. After oxidation, a mass of oxygen-containing groups are introduced, inducing an oxygen-enriched carbon precursor. During the high-temperature carbonization, the precursor first liberates more volatile substances to lose hydrogen, forming a strongly cross-linked, open-structured, non-graphitizing carbon. As the carbonization temperature gradually increases, the pitch-based carbon maintains the non-graphitizing structure until the heating finishes and exhibits the outstanding reversible capacity and ICE.

On the contrary, when the pyrolysis temperature is higher than $T_p$, pitch turns to completely carbonized pitch and begins to form ordered carbon layers due to excess hydrogen. The subsequent oxidation is too late to transform the fusion-state into solid-state carbonization, only increasing a number of oxygen-containing groups, most of which are also decomposed into volatile substances during the high-temperature carbonization. It is a process of gradually graphitized for pitch with limited oxygen increase and electrochemical performances improvement.

## Conclusions

A series of pitch-based carbon for SIB anodes via low-temperature pyrolysis, oxidation, and high-temperature carbonization were prepared. We adopted a precise low-temperature pyrolysis strategy, which adjusted the pyrolysis temperature over a wide range of $0 \sim 800$ °C, to affirm the effective oxidation precursor. The microstructure of pitch-based carbon was characterized by HRTEM, XRD, Raman, TG, FTIR, and XPS. The Na storage behaviors and performances were evaluated by galvanostatic charge/discharge, CV, cycle, rate, and EIS measurements. Based on the evolution of the Na storage behavior with the microstructure, the following insights about the carbonized oxidized pitch are proposed. First, not all the oxidations can restrain the graphitization of pitch and enhance Na storage performances, which is only effective for incompletely carbonized pitch. Second, whether or not oxidation is effective, oxygen is introduced into carboxyl in different amounts. Third, when the precursor is incompletely

**Fig. 7** Schematic comparison of carbonized pristine pitch and carbonized oxidized pitch
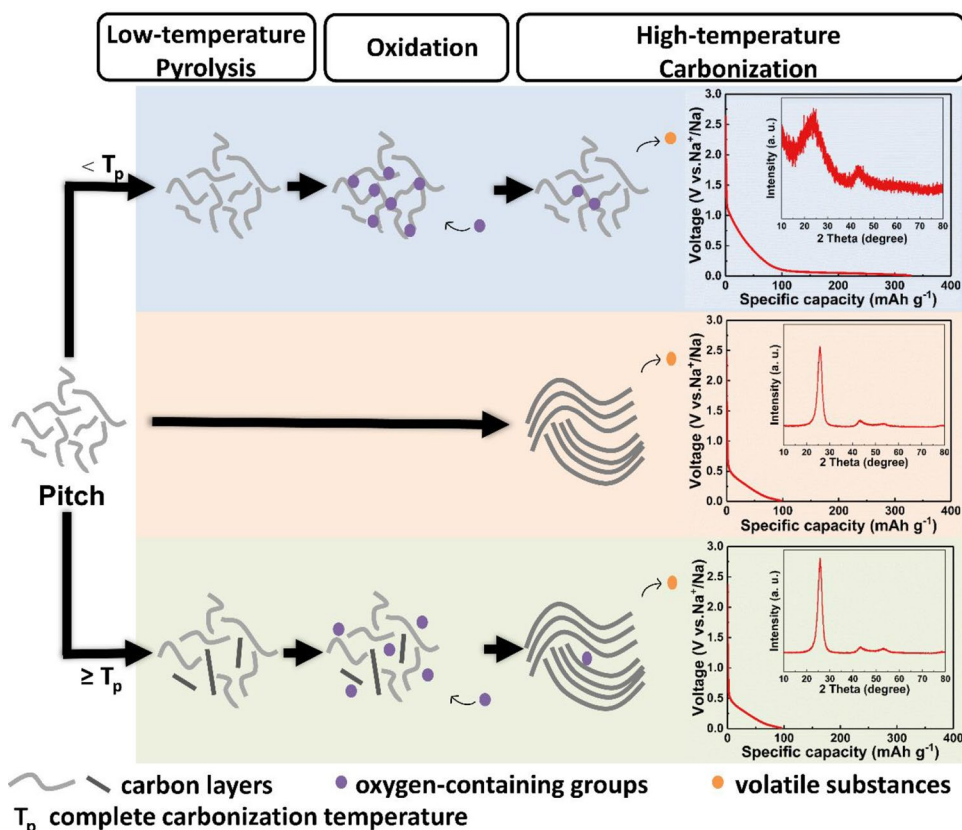
carbonized pitch, the carbonized oxidized pitch is an amorphous structure, whose electrochemical performances have been greatly improved with a 0.1 V voltage plateau. Fourth, when the precursor is completely carbonized pitch, the carbonized oxidized pitch is a graphite-like microcrystallite structure with limited effect on the electrochemical performances in SIB.

The "only incompletely carbonized pitch can be effective oxidized" behavior more clearly illustrates the nature of oxidation to suppress the graphitization and enhance Na storage performances. Carbon material can remain an amorphous structure at high temperature as long as the hydrogen content is reduced before complete carbonization. Oxidation should not be the only way to lose hydrogen through releasing volatile substances. The introduction of other elements to lose hydrogen through releasing volatiles with hydrogen is worthy of further exploration and research, which presents a new insight into the design and development of advanced soft carbon anode materials for SIB.

# References

1. Palomares V, Serras P, Villaluenga I, Hueso KB, Carretero-González J, Rojo T (2012) Na-ion batteries, recent advances and present challenges to become low cost energy storage systems. Energy Environ Sci 5(3):5884–5901

2. Wu F, Liu J (2020) Energy material advances: from fundamental discoveries to practical applications. Energy Mater Adv 2020:7981289

3. Armand M, Tarascon JM (2008) Building better batteries. Nature 451(7179):652–657

4. Pan HL, Hu YS, Chen LQ (2013) Room-temperature stationary sodium-ion batteries for large-scale electric energy storage. Energy Environ Sci 6(8):2338–2360

5. Yang ZG, Zhang JL, Kintner-Meyer MCW, Lu XC, Choi D, Lemmon JP, Liu J (2011) Electrochemical energy storage for green grid. Chem Rev 111(5):3577–3613

6. Saurel D, Orayech B, Xiao BW, Carriazo D, Li XL, Rojo T (2018) From charge storage mechanism to performance: a roadmap toward high specific energy sodium-ion batteries through carbon anode optimization. Adv Energy Mater 8(17):1703268

7. Doeff MM, Ma YP, Visco SJ, De Jonghe LC (1993) Electrochemical insertion of sodium into carbon. J Electrochem Soc 140(12):L169–L170

8. Stevens DA, Dahn JR (2000) High capacity anode materials for rechargeable sodium-ion batteries. J Electrochem Soc 147(4):1271–1273

9. Thomas P, Billaud D (2002) Electrochemical insertion of sodium into hard carbons. Electrochim Acta 47(20):3303–3307

10. Alvin S, Yoon D, Chandra C, Cahyadi HS, Park J-H, Chang WY, Chung KY, Kim J (2019) Revealing sodium ion storage mechanism in hard carbon. Carbon 145:67–81

11. Dong RQ, Wu F, Bai Y, Li QH, Yu XQ, Li Y, Ni Q, Wu C (2022) Tailoring defects in hard carbon anode towards enhanced Na storage performance. Energy Mater Adv 2022:9896218

12. Feng X, Bai Y, Zheng LM, Liu MQ, Li Y, Zhao R, Li Y, Wu C (2021) Effect of different nitrogen configurations on sodium storage properties of carbon anodes for sodium ion batteries. ACS Appl Mater Interfaces 13(47):56285–56295

13. Voronina N, Myung ST (2021) Recent advances in electrode materials with anion redox chemistry for sodium-ion batteries. Energy Mater Adv 2021:9819521

14. Jin HL, Feng X, Li J, Li M, Xia YZ, Yuan YF, Yang C, Dai B, Lin ZQ, Wang JC, Lu J, Wang S (2019) Heteroatom-doped porous carbon materials with unprecedented high volumetric capacitive performance. Angew Chem Int Ed 58(8):2397–2401

15. Feng X, Bai Y, Liu MQ, Li Y, Yang HY, Wang XR, Wu C (2021) Untangling the respective effects of heteroatom-doped carbon materials in batteries, supercapacitors and the ORR to design high performance materials. Energy Environ Sci 14(4):2036–2089

16. Chen H, Sun N, Zhu QZ, Soomro RA, Xu B (2022) Microcrystalline hybridization enhanced coal-based carbon anode for advanced sodium-ion batteries. Adv Sci 9:2200033

17. Zhao R, Sun N, Xu B (2021) Recent advances in heterostructured carbon materials as anodes for sodium-ion batteries. Small Struct 2(12):2100132

18. Sun N, Guan ZRX, Liu YW, Cao YL, Zhu QZ, Liu H, Wang ZX, Zhang P, Xu B (2019) Extended "adsorption-insertion" model: a new insight into the sodium storage mechanism of hard carbons. Adv Energy Mater 9(32):1901351

19. Lu P, Sun Y, Xiang HF, Liang X, Yu Y (2018) 3D amorphous carbon with controlled porous and disordered structures as a high-rate anode material for sodium-ion batteries. Adv Energy Mater 8(8):1702434

20. Yao XH, Ke YJ, Ren WH, Wang XP, Xiong FY, Yang W, Qin MS, Li Q, Mai LQ (2019) Defect-rich soft carbon porous nanosheets for fast and high-capacity sodium-ion storage. Adv Energy Mater 9(6):1803260

21. Xie F, Xu Z, Jensen ACS, Au H, Lu YX, Araullo-Peters V, Drew AJ, Hu YS, Titirici M-M (2019) Hard-soft carbon composite anodes with synergistic sodium storage performance. Adv Funct Mater 29(24):1901072

22. Xie F, Niu YS, Zhang QQ, Guo ZY, Hu ZL, Zhou Q, Xu Z, Li YQ, Yan RT, Lu YX, Titirici M-M, Hu YS (2022) Screening heteroatom configurations for reversible sloping capacity promises high-power Na-ion batteries. Angew Chem Int Edit 61(11):e202116394

23. Liu SY, Shao WL, Zhang WS, Zhang TP, Song C, Yao M, Huang H, Jian XG, Hu FY (2021) Regulating microstructures of soft carbon anodes by terminations of $Ti_3C_2T_X$ MXene toward fast and stable sodium storage. Nano Energy 87:106097

24. Jian ZL, Bommier C, Luo LL, Li ZF, Wang WT, Wang CM, Greaney PA, Ji XL (2017) Insights on the mechanism of Na-ion storage in soft carbon anode. Chem Mater 29(5):2314–2320

25. Li YM, Hu YS, Li H, Chen LQ, Huang XJ (2016) A superior low-cost amorphous carbon anode made from pitch and lignin for sodium-ion batteries. J Mater Chem A 4(1):96–104

26. Luo W, Jian ZL, Xing ZY, Wang W, Bommier C, Lemer MM, Ji XL (2015) Electrochemically expandable soft carbon as anodes for Na-ion batteries. ACS Central Sci 1(9):516–522

27. Cao B, Liu H, Xu B, Lei YF, Chen XH, Song HH (2016) Mesoporous soft carbon as an anode material for sodium ion batteries with superior rate and cycling performance. J Mater Chem A 4(17):6472–6478

28. Pol VG, Lee E, Zhou DH, Dogan F, Calderon-Moreno JM, Johnson CS (2014) Spherical carbon as a new high-rate anode for sodium-ion batteries. Electrochim Acta 127(1):61–67

29. Mochida I, Korai Y, Ku CH, Watanabe F, Sakai Y (2000) Chemistry of synthesis, structure, preparation and application of aromatic-derived mesophase pitch. Carbon 38(2):305–328

30. Wang QD, Zhao CL, Lu YX, Li YM, Zheng YH, Qi YR, Rong XH, Jiang LW, Qi XG, Shao YJ, Pan D, Li BH, Hu YS, Chen LQ (2017) Advanced nanostructured anode materials for sodium-ion batteries. Small 13(42):1701835

31. Jiang MC, Sun N, Soomro RA, Xu B (2021) The recent progress of pitch-based carbon anodes in sodium-ion batteries. J Energy Chem 55:34–47

32. Kipling JJ, Sherwood JN, Shooter PV, Thompson NR (1964) Factors influencing the graphitization of polymer carbons. Carbon 1(3):315–320

33. Miura K, Nakagawa H, Hashimoto K (1995) Examination of the oxidative stabilization reaction of the pitch-based carbon fiber through continuous measurement of oxygen chemisorption and gas formation rate. Carbon 33(3):275–282

34. Barr JB, Lewis IC (1978) Chemical changes during the mild air oxidation of pitch. Carbon 16(6):439–444

35. Lu YX, Zhao CL, Qi XG, Qi YR, Li H, Huang XJ, Chen LQ, Hu YS (2018) Pre-oxidation-tuned microstructures of carbon anodes derived from pitch for enhancing Na storage performance. Adv Energy Mater 8(27):1800108

36. Hou BH, Wang YY, Ning QL, Li WH, Xi XT, Xu Y, Liang HJ, Feng X, Wu XL (2019) Self-supporting, flexible, additive-free, and scalable hard carbon paper self-interwoven by 1D microbelts: superb room/low-temperature sodium storage and working mechanism. Adv Mater 31(40):1903125

37. Franklin RE (1951) Crystallite growth in graphitizing and non-graphitizing carbons. Proc R Soc Lon Ser-A 209(1097):196–218

38. Kipling JJ, Sherwood JN, Shooter PV, Thompson NR (1964) The pore structure and surface area of high-temperature polymer carbons. Carbon 1(3):321–328

39. Gilbert JB, Kipling JJ, McEnaney B, Sherwood JN (1962) Carbonization of polymers I—thermogravimetric analysis. Polymer 3:1–10

40. Qi YR, Lu YX, Liu LL, Qi XG, Ding FX, Li H, Huang XJ, Chen LQ, Hu YS (2020) Retarding graphitization of soft carbon precursor: from fusion-state to solid-state carbonization. Energy Storage Mater 26:577–584

41. Franklin RE (1951) The structure of graphitic carbons. Acta Crystallorg 4(3):253–261

42. Cowlard FC, Lewis JC (1967) Vitreous carbon—a new form of carbon. J Mater Sci 2(6):507–512

43. Harris PJF, Tsang SC (1997) High-resolution electron microscopy studies of non-graphitizing carbons. Philos Mag A 76(3):667–677

44. Stevens DA, Dahn JR (2001) The mechanisms of lithium and sodium insertion in carbon materials. J Electrochem Soc 148(8):A803–A811

45. Li ZY (2017) Pyrolysis behavior and reactivity of carbon anode materials of aluminum electrolysis. Chongqing University, Chongqing

46. Qi YR, Lu YX, Ding FX, Zhang QQ, Li H, Huang XJ, Chen LQ, Hu YS (2019) Slope-dominated carbon anode with high specific capacity and superior rate capability for high safety Na-ion batteries. Angew Chem Int Edit 58(13):4361–4365

47. Al-Gaashani R, Najjar A, Zakaria Y, Mansour S, Atieh MA (2019) XPS and structural studies of high quality graphene oxide and reduced graphene oxide prepared by different chemical oxidation methods. Ceram Int 45(11):14439–14448

48. Sun F, Wang H, Qu ZB, Wang KF, Wang LJ, Gao JH, Gao JM, Liu SQ, Lu YF (2021) Carboxyl-dominant oxygen rich carbon for improved sodium ion storage: synergistic enhancement of adsorption and intercalation mechanisms. Adv Energy Mater 11(1):2002981

49. Wepasnick KA, Smith BA, Schrote KE, Wilson HK, Diegelmann SR, Fairbrother DH (2011) Surface and structural characterization of multi-walled carbon nanotubes following different oxidative treatments. Carbon 49(1):24–36

50. Drbohlav J, Stevenson WTK (1995) The oxidative stabilization and carbonization of a synthetic mesophase pitch, part II: the carbonization process. Carbon 33(5):713–731

51. Li YM (2017) Studies on carbon-based anode materials for sodium-ion stationary batteries. University of Chinese Academy of Sciences, Beijing

52. Qiu S, Xiao LF, Sushko ML, Han KS, Shao YY, Yan MY, Liang XM, Mai LQ, Feng JW, Cao YL, Ai XP, Yang HX, Liu J (2017) Manipulating adsorption-insertion mechanisms in nanostructured carbon materials for high-efficiency sodium ion storage. Adv Energy Mater 7(17):1700403

53. Lu Y, Shin KH, Yu YF, Hu YZ, Liang JN, Chen K, Yuan HC, Park HS, Wang D (2021) Multiple active sites carbonaceous anodes for Na⁺ storage: synthesis, electrochemical properties and reaction mechanism analysis. Adv Funct Mater 31(12):2007247

54. Yun BN, Du HL, Hwang JY, Jung HG, Sun YK (2017) Improved electrochemical performance of boron-doped carbon-coated lithium titanate as an anode material for sodium-ion batteries. J Mater Chem A 5(6):2802–2810

55. Li XJ, Lei Y, Qin L, Han D, Wang HW, Zhai DY, Li BH, Kang FY (2021) Mildly-expanded graphite with adjustable interlayer distance as high-performance anode for potassium-ion batteries. Carbon 172:200–206

56. Jian ZL, Luo W, Ji XL (2015) Carbon electrodes for K-ion batteries. J Am Chem Soc 137(36):11566–11569

57. Kim H, Kim JC, Bianchini M, Seo DH, Rodriguez-Garcia J (2018) Recent progress and perspective in electrode materials for K-ion batteries. Adv Energy Mater 8(9):1702384

58. Xu JT, Dou YH, Wei ZX, Mai LQ, Deng YH, Li YT, Liu HK, Dou SX (2017) Recent progress in graphite intercalation compounds for rechargeable metal (Li, Na, K, Al)-ion batteries. Adv Sci 4(10):1700146

59. Zhang LP, Wang W, Lu SF, Xiang Y (2021) Carbon anode materials: a detailed comparison between Na-ion and K-ion batteries. Adv Energy Mater 11(11):2003640

60. Rajagopalan R, Tang YG, Ji XB, Jia CK, Wang HY (2020) Advancements and challenges in potassium ion batteries: a comprehensive review. Adv Funct Mater 30(12):1909486

61. Luo W, Wan JY, Ozdemir B, Bao WZ, Chen YN, Dai JQ, Lin H, Xu Y, Gu F, Barone V, Hu LB (2015) Potassium ion batteries with graphitic materials. Nano Lett 15(11):7671–7677

62. Zhao J, Zou XX, Zhu YJ, Xu YH, Wang CS (2016) Electrochemical intercalation of potassium into graphite. Adv Funct Mater 26(44):8103–8110

63. Liu MQ, Wang YH, Wu F, Bai Y, Li Y, Gong YT, Feng X, Li Y, Wang XR, Wu C (2022) Advances in carbon materials for sodium and potassium storage. Adv Funct Mater 32:2203117

64. Jian ZL, Hwang S, Li ZF, Hernandez AS, Wang XF, Xing ZY, Su D, Ji XL (2017) Hard-soft composite carbon as a long-cycling and high-rate anode for potassium-ion batteries. Adv Funct Mater 27(26):1700324

65. Cao W, Zhang EJ, Wang J, Liu ZM, Ge JM, Yu XZ, Yang HG, Lu BG (2019) Potato derived biomass porous carbon as anode for potassium ion batteries. Electrochim Acta 293(10):364–370

66. Liu Y, Lu YX, Xu YS, Meng QS, Gao JC, Sun YG, Hu YS, Chang BB, Liu CT, Cao AM (2020) Pitch-derived soft carbon as stable anode material for potassium ion batteries. Adv Mater 32(17):2000505

67. Wang LP, Yang JY, Li J, Chen T, Chen SL, Wu ZR, Qiu JL, Wang BJ, Gao P, Niu XB, Li H (2019) Graphite as a potassium ion battery anode in carbonate-based electrolyte and ether-based electrolyte. J Power Sources 409(1):24–30